

The Role of Attenuated Astrocyte Activation in Infantile Neuronal Ceroid Lipofuscinosis

Shannon L. Macauley,¹ Milos Pekny,³ and Mark S. Sands^{1,2}

Departments of ¹Internal Medicine and ²Genetics, Washington University School of Medicine, St. Louis, Missouri 63110, and ³Center for Brain Repair and Rehabilitation, Department of Clinical Neuroscience and Rehabilitation, Institute of Neuroscience and Physiology, Sahlgrenska Academy at the University of Gothenburg, 41390 Gothenburg, Sweden

Infantile neuronal ceroid lipofuscinosis (INCL) is an inherited neurodegenerative disorder affecting the CNS during infancy. INCL is caused by mutations in the *CLN1* gene that lead to a deficiency in the lysosomal hydrolase, palmitoyl protein thioesterase 1 (PPT1). A murine model of INCL, the PPT1-deficient (*PPT1*^{-/-}) mouse, is an accurate phenocopy of the human disease. The first pathological change observed in the *PPT1*^{-/-} brain is regional areas of glial fibrillary acidic protein (GFAP) upregulation, which predicts future areas of neurodegeneration. We hypothesized that preventing GFAP and vimentin upregulation in reactive astrocytes will alter the CNS disease. To test this hypothesis, we generated mice simultaneously carrying null mutations in the *GFAP*, *Vimentin*, and *PPT1* genes (*GFAP*^{-/-}*Vimentin*^{-/-}*PPT1*^{-/-}). Although the clinical and pathological features of the *GFAP*^{-/-}*Vimentin*^{-/-}*PPT1*^{-/-} mice are similar to INCL, the disease appears earlier and progresses more rapidly. One mechanism underlying this accelerated phenotype is a profound neuroinflammatory response within the CNS. Thus, our data identify a protective role for intermediate filament upregulation during astrocyte activation in INCL, a model of chronic neurodegeneration.

Introduction

Infantile neuronal ceroid lipofuscinosis (INCL), or Batten disease, is an autosomal-recessive, lysosomal storage disease affecting the CNS (Kohlschütter et al., 1993; Hofmann et al., 1999). Caused by a deficiency in palmitoyl protein thioesterase 1 (PPT1) (Vesa et al., 1995; Hofmann et al., 2001), INCL patients are asymptomatic at birth and develop normally until they present with visual impairments, seizures, cognitive deficits, and motor dysfunction. Death occurs by 6 years (Santavuori et al., 1973; Santavuori et al., 1974). Pathological findings include autofluorescent storage material, glial activation, brain atrophy, cortical thinning, neuronal loss, and demyelination (Haltia et al., 1973a,b). A PPT1-deficient (*PPT1*^{-/-}) mouse model was generated by disrupting the *CLN1* gene (Gupta et al., 2001) and mimics the cellular pathology and functional deficits observed in INCL patients (Bible et al., 2004; Griffey et al., 2004, 2005, 2006; Kielar et al., 2007; Macauley et al., 2009).

Previous studies demonstrated that localized regions of increased expression of an intermediate filament protein glial fibrillary acidic protein (GFAP) expression are the first pathological changes observed in the *PPT1*^{-/-} brains (Kielar et al., 2007; Macauley et al., 2009). These regions also suffer the greatest neuronal loss and atrophy as the disease progresses. We hypothesize that the upregulation of intermediate filament proteins in reactive astrocytes plays an active role in the pathogenesis of INCL.

The role of intermediate filament upregulation is an incompletely understood phenomenon in CNS disease (Kalman, 2004; Pekny and Nilsson, 2005; Sofroniew, 2005). Although GFAP upregulation is a common indicator of reactive astrocytes, the relationship between increased intermediate filament protein expression (i.e., GFAP, vimentin, and nestin) during astrocyte hypertrophy and functional changes at the molecular level remains unclear. Given the elaborate set of functions associated with reactive astrocytes, and others described astrocyte activation as both a gain and loss of function phenomenon resulting in favorable and deleterious effects to an injured CNS, based on data gathered from numerous transgenic mouse studies (Pekny and Nilsson, 2005; Sofroniew et al., 2009; Sofroniew and Vinters, 2010). Mice deficient in astrocyte intermediate filament proteins, GFAP and vimentin (Vim), address the relationship between structural alterations and functional changes associated with astrocyte activation, and report both positive (e.g., axonal sprouting, synaptic regeneration, faster wound healing, decreased immune cell infiltration) and negative (e.g., disrupted glial scars, larger infarct volumes, increased cell death) outcomes when challenged (Pekny et al., 1995, 1999; Lane and Pekny, 2004; Lundkvist et al., 2004; Pekny and Pekna, 2004; Nakazawa et al., 2007; Li et al., 2008; Verardo et al., 2008). Thus, it is difficult to predict what role GFAP upregulation in the CNS plays in INCL.

Received July 13, 2011; revised Sept. 8, 2011; accepted Sept. 13, 2011.

Author contributions: S.L.M. and M.S.S. designed research; S.L.M. performed research; M.P. contributed unpublished reagents/analytic tools; S.L.M. analyzed data; S.L.M. wrote the paper.

This work was supported by NIH Grant NS043105 (M.S.S.), ALF Göteborg (M.P.), the Swedish Medical Research Council (Project 11548; M.P.), Ruth L. Kirschstein National Research Service Award Fellowship NS056728 (S.L.M.), and a postdoctoral research fellowship from the Batten Disease Support and Research Association (S.L.M.). Also, we would like to acknowledge support from the Ruwitch Foundation (M.S.S.). We thank Adarsh Reddy for his help with statistical analysis; Kevin O'Dell and Beth Eultgen for their work in animal husbandry; Corinne Cusumano for help with the confocal microscope; and Neuroscience Associates (Knoxville, TN) for their consistent quality of silver degeneration staining. Further, we would like to acknowledge Jin Moo Lee and Ulrika Wilhelmsson for their comments on this manuscript.

Correspondence should be addressed to Mark S. Sands, Washington University School of Medicine, Department of Internal Medicine, Campus Box 8007, 660 S. Euclid Avenue, St. Louis, MO 63110. E-mail: msands@dom.wustl.edu or msands@dom.wustl.edu.

DOI:10.1523/JNEUROSCI.3579-11.2011

Copyright © 2011 the authors 0270-6474/11/3115575-11\$15.00/0

For the purposes of our studies, we used mice deficient in GFAP and Vimentin ($GFAP^{-/-}Vim^{-/-}$) as a model of attenuated astrocyte activation. By crossing the $GFAP^{-/-}Vim^{-/-}$ mice with the $PPT1^{-/-}$ mice, we were able to study the role of attenuated astrocyte activation in INCL. In the $GFAP^{-/-}Vim^{-/-}PPT1^{-/-}$ brains, the course of disease is exacerbated compared with $PPT1^{-/-}$ mice. Mechanisms responsible for this accelerated phenotype include immune cell infiltration and cytokine upregulation. These data suggest that astrocyte activation plays a protective role in INCL.

Materials and Methods

GFAP^{-/-}Vim^{-/-}PPT1^{-/-} mice. The individual $GFAP^{-/-}Vim^{-/-}$ and $PPT1^{-/-}$ mice were created as previously reported (Colucci-Guyon et al., 1994; Pekny et al., 1995, 1999; Eliasson et al., 1999; Gupta et al., 2001; Griffey et al., 2005). The $GFAP^{-/-}Vim^{-/-}$ mice were of a mixed C57BL/6/129SV/129Ola background, and the $PPT1^{-/-}$ mice were of a congenic C57BL/6 background. The homozygous $GFAP^{-/-}Vim^{-/-}$ mice were crossed with the homozygous $PPT1^{-/-}$ mice for the first initial mating. The heterozygous progeny ($GFAP^{+/-}Vim^{+/-}PPT1^{+/-}$) of the initial mating were backcrossed to the $PPT1^{-/-}$ background for two additional generations, producing an 88% C57BL/6 background. Then, the heterozygous $GFAP^{+/-}Vim^{+/-}PPT1^{+/-}$ offspring were intercrossed to ultimately generate all four groups ($GFAP^{-/-}Vim^{-/-}PPT1^{-/-}$, $GFAP^{-/-}Vim^{-/-}$, $PPT1^{-/-}$, and WT). For the purposes of our studies, the mice were all generationally matched and maintained as four distinct homozygous lines. The only exception was that the silver degeneration staining was performed on $PPT1^{-/-}$ and WT mice with a congenic C57BL/6 background. All mice were maintained at Washington University School of Medicine. Mouse genotypes were determined by PCR-based assays. Both male and female mice from each genotype were used in this study. Animals were housed under a 12 h light/dark cycle and were provided food and water *ad libitum*. All procedures were performed under an approved Institutional Animal Care and Use Committee protocol from Washington University School of Medicine.

Longevity. $GFAP^{-/-}Vim^{-/-}PPT1^{-/-}$, $GFAP^{-/-}Vim^{-/-}$, $PPT1^{-/-}$, and WT mice ($n = 10$ – 18 mice per genotype) were used to assess lifespan. Mice from each group were allowed to age, unmanipulated, under the conditions described above. The end of life was signaled by either death or a predetermined moribund condition. Kaplan–Meier analysis was used to measure cumulative survival and determine differences ($p < 0.05$) in lifespan.

Brain weights. The 3-, 5-, and 6-month-old $GFAP^{-/-}Vim^{-/-}PPT1^{-/-}$, $GFAP^{-/-}Vim^{-/-}$, $PPT1^{-/-}$, and WT mice ($n = 5$ – 6 mice/genotype/age) were killed via an overdose of euthasol, and the brains were harvested by a researcher blinded to both age and genotype. A razor blade was inserted coronally between the forebrain and olfactory bulbs to remove the olfactory bulbs from the remainder of the brain. Similarly, a coronal cut was made immediately posterior to the cerebellum to remove the medulla and spinal cord from the forebrain and cerebellum. Each brain was weighed. Differences in weights were analyzed with one-way ANOVAs followed by Bonferroni's correction *post hoc* tests.

Autofluorescent accumulation. Six-month-old $GFAP^{-/-}Vim^{-/-}PPT1^{-/-}$, $GFAP^{-/-}Vim^{-/-}$, $PPT1^{-/-}$, and WT mice ($n = 3$ mice per group) were used to quantify autofluorescent accumulation in the somatosensory barrel field (S1BF) cortex using epifluorescent microscopy (Bible et al., 2004; Kielar et al., 2007). Briefly, mice were given an overdose of euthasol, and the brains were removed and fixed for 48 h in 4% PFA in phosphate buffer. Following fixation, the brains were cryoprotected in 30% sucrose, embedded in optimal cutting temperature compound (OCT; Sakura), and sectioned coronally on a freezing cryostat at 20 μ m thickness. Images from three serial sections through S1BF for each group were captured via a 20 \times objective and FITC filter on a Nikon microscope with a SPOT camera attached. All variables associated with image capture, including exposure time, binning, and gain, were held constant for all groups. Using ImageJ software, threshold analysis was performed to determine which pixels contained autofluorescent accumulation in a given image. The percentage of pixels containing autofluo-

rescent material was calculated for each image and reported as the area fraction. Three sets of area fraction measurements were captured for each of the three sections through S1BF in each of the four groups. The average for each group was calculated. Differences in autofluorescent accumulation were analyzed using a one-way ANOVA followed by Bonferroni's correction *post hoc* test.

Nissl staining. Nissl staining was performed on 6-month-old $GFAP^{-/-}Vim^{-/-}PPT1^{-/-}$, $GFAP^{-/-}Vim^{-/-}$, $PPT1^{-/-}$, and WT mice ($n = 3$ mice per group). Briefly, mice were given a lethal injection of euthasol, the brains removed, fixed for 48 h in 4% PFA in phosphate buffer, cryoprotected in 30% sucrose, embedded in OCT, and sectioned coronally on a freezing cryostat at 20 μ m thickness. Sections throughout the primary visual cortex (V1) were mounted on glass slides, placed on a warming plate for 1 h and allowed to thoroughly dry overnight at room temperature. Sections were briefly rinsed in distilled H₂O (dH₂O), incubated in 0.5% cresyl violet for 2 min, and rinsed with dH₂O. The sections were then dehydrated via a series of alcohols and xylenes, and coverslipped.

Cortical thickness. Cortical thickness measurements were performed on Nissl-stained tissue from $GFAP^{-/-}Vim^{-/-}PPT1^{-/-}$, $GFAP^{-/-}Vim^{-/-}$, $PPT1^{-/-}$ and WT brains ($n = 3$ brains per group). Images throughout V1 were captured at 10 \times magnification using an Olympus BX41 microscope and Olympus DP 20 camera. Cortical thickness measurements were made by an observer blinded to genotype from the boundary of the white matter to the pial surface for each brain, as delineated by Paxinos and Franklin (1997) and as previously described (Bible et al., 2004; Kielar et al., 2007). A series of 10 individual measurements was made for each of three sections for each mouse ($n = 3$ mice per group). For each mouse, the mean cortical thickness measurement for each section was calculated, and statistical significance was performed by a one-way ANOVA followed by Bonferroni's correction *post hoc* test.

de Olmos cupric-silver staining. Three-, 5-, and 6-month-old $GFAP^{-/-}Vim^{-/-}PPT1^{-/-}$, $GFAP^{-/-}Vim^{-/-}$, $PPT1^{-/-}$, and WT mice ($n = 2$ per time point) were processed for de Olmos silver staining. Briefly, the mice were deeply anesthetized with euthasol and transcardially perfused with 4% paraformaldehyde in sodium cacodylate buffer. The brains were removed and postfixed for 48 h. Each brain was embedded in a gelatin-based matrix (Switzer, 2000), and serial coronal sections (35 μ m) were made on a freezing microtome by Neuroscience Associates. Neuronal degeneration was visualized by staining with a modified de Olmos cupric-silver method (DeOlmos and Ingram, 1971; Switzer, 2000). A matrix of brains at identical levels in the coronal plane was stained simultaneously.

Blood–brain barrier permeability. Blood–brain barrier (BBB) integrity was assessed in 5-month-old WT and $GFAP^{-/-}Vim^{-/-}PPT1^{-/-}$ ($n = 4$ mice per group) using an Evan's blue (EB) assay (Belayev et al., 1996; Young et al., 2004). $PPT1$ -deficient mice receiving a middle cerebral artery occlusion (MCAO) served as a positive control. Mice were injected with 2% Evan's blue in saline via a tail vein injection (4 μ l/g body weight). After 30 min, the mice were transcardially perfused with PBS until both the perfusate and liver were clear of blood (~ 1 – 2 min). The brains were removed, bisected sagittally, and weighed. One hemisphere was placed in 500 μ l of 50% TCA solution and homogenized for 1 min. Following centrifugation, the dye was extracted and diluted 1:3 in EtOH. To determine the concentration of Evan's blue dye in samples, the fluorescence of each sample was determined by a fluorescent spectrophotometer (F-2000, Hitachi; excitation of 620 nm and emission at 680 nm), and the concentration was calculated based on external standards (100–500 ng/ml) per gram of tissue. A one-way ANOVA was performed to determine statistical significance at the $p < 0.05$ level, with Tukey's multiple-comparison's *post hoc* test.

Middle cerebral artery occlusion. Middle cerebral artery (MCA) occlusion was achieved using a nylon suture for 60 min as described previously (Belayev et al., 1996). Using an operating microscope, the left external carotid artery (ECA) was exposed and loosely ligated with a 5–0 silk suture through a midline neck incision in anesthetized mice. The distal stump of the ECA and the branches to the proximal stump were electrocoagulated. A 12 mm 6–0 surgical monofilament nylon suture was introduced into the ECA stump, advanced 9–10 mm from the bifurcation of the common carotid artery into the circle of Willis to occlude the

ostium of the MCA to cause a 20% decrease in laser Doppler signal. The 6–0 silk suture ligating the proximal ECA was tightened to prevent bleeding and immobilize the intraluminal suture inserted into the MCA. Mice were transferred to an incubator (32°C) and allowed to recover from anesthesia. After 60 min, ischemia will be terminated by removal of the intraluminal suture. Restoration of blood flow through the internal carotid artery following removal of the intraluminal suture will be confirmed directly under an operating microscope and more distally by laser Doppler (Miller et al., 2001; Gidday et al., 2005).

Immunohistochemistry. Six-month-old $GFAP^{-/-}Vim^{-/-}PPT1^{-/-}$, $GFAP^{-/-}Vim^{-/-}$, $PPT1^{-/-}$, and WT mice were killed via an overdose of euthasol and transcardially perfused with PBS until the liver was clear of blood. The brains were removed and fixed in 4% paraformaldehyde in phosphate buffer for 48 h, were cryoprotected with 30% sucrose in Tris-buffered saline (TBS), and embedded in OCT. Brains were sectioned in the coronal plane throughout the rostral–caudal axis using a freezing cryostat. Adjacent, free-floating sections were incubated with the following antibodies: rabbit anti-GFAP (1:500; Immunostar); rat anti-CD68 (1:500; AbD, Serotec); rat anti-CD31 [1:50; platelet endothelial cell adhesion molecule-1 (PECAM), BD PharMingen]; rat anti-CD45 (1:50; BD PharMingen); rabbit anti-CD3 (1:200; Laboratory Vision); and rabbit anti-aquaporin 4 (AQP4; 1:1000; Millipore Bioscience Research Reagents). Briefly, sections were washed in TBS, incubated in 1% H_2O_2 (Sigma) to quench endogenous peroxidase activity, and rinsed thoroughly in TBS. The tissue was blocked for 1 h in 10% normal goat serum (NGS; Sigma) and 0.25% Triton X-100 in TBS. Sections were incubated overnight at 4°C with primary antibodies in 5% NGS and 0.2% Triton X-100 in TBS. The following day the sections were rinsed in TBS and incubated with secondary antibodies (1:500–1000, Vector Laboratories; or 1:500, Invitrogen) in 10% NGS and 0.1% Triton X-100 in TBS for 75 min. The tissue was rinsed with TBS and then incubated with a peroxidase-conjugated avidin–biotin complex (1:100; Vectastain Elite ABC kit, Vector Laboratories) for 1 h at room temperature. Antibody immunoreactivity was visualized with 3′-3′ diaminobenzidine and H_2O_2 (DAB kit, Vector Laboratories) in TBS. Sections were dehydrated and coverslipped.

Quantitation for CD68-positive cells was performed in the S1BF cortex of 6-month-old WT, $GFAP^{-/-}Vim^{-/-}$, $PPT1^{-/-}$, and $GFAP^{-/-}Vim^{-/-}PPT1^{-/-}$ brains. Images through the S1BF were captured using a 20× objective, Olympus BX41 microscope and Olympus DP 20 camera. All variables associated with image capture were held constant. Using ImageJ software, images were converted to 8-bit grayscale, and threshold analysis was used to identify CD68-positive cell bodies within the cortex. Cell counts were performed on three sets of images taken per section, on three sections total from three different brains per each genotype ($n = 4$). Statistical significance was calculated using a one-way ANOVA followed by Tukey's *post hoc* test.

To quantify CD3-positive cells, images were captured in the S1BF cortex of 6-month-old WT, $GFAP^{-/-}Vim^{-/-}$, $PPT1^{-/-}$, and $GFAP^{-/-}Vim^{-/-}PPT1^{-/-}$ brains. Images through the S1BF were captured using a 20× objective, Olympus BX41 microscope and Olympus DP 20 camera, where all variables associated with image capture were held constant. Manual cell counts were performed on three sets of images taken per section, on three sections total from three different brains per each of four genotypes. Statistical significance was calculated using a one-way ANOVA followed by Tukey's *post hoc* test.

Cytokine assays. To quantify the concentration of chemokines and cytokines within the brain, a 14-biomarker Multi-Analyte Profile was generated for 1-, 3-, and 6-month-old $GFAP^{-/-}Vim^{-/-}PPT1^{-/-}$, $PPT1^{-/-}$, $GFAP^{-/-}Vim^{-/-}$, and WT mice by MYRIAD RBM using standard Luminex technology. The 14 analytes included the following: FGF-9, granulocyte-macrophage colony-stimulating factor (GM-CSF), interferon- γ (IFN- γ), IFN- γ -induced protein 10 [IP-10 (or CXCL10)], lymphotactin (XCL1), macrophage inflammatory protein-1 β [MIP-1 β (or CCL4)], MIP-2 (CXCL1), monocyte chemoattractant protein-1 [MCP-1 (or CCL2)], MCP-3 (or CCL7), MCP-5 (or CCL12), oncostatin-M, RANTES [regulated upon activation, normal T-cell expressed and secreted (or CCL5)], and tumor necrosis factor- α (TNF- α). Briefly, mice were transcardially perfused with PBS, and the brains were homogenized

in a solution consisting of 10 mM Tris, 150 mM NaCl, 1 mM dithiothreitol, 0.2% Triton, and 20 μ l/ml protease inhibitor cocktail (Sigma). The supernatant from brain homogenates was diluted to obtain a protein target concentration of 0.5–1.0 mg/ml and stored at $-70^{\circ}C$. Cytokine concentrations were quantified according to standard protocols at MYRIAD RBM. A one-way ANOVA followed by Bonferroni's *post hoc* tests was used to determine significant changes in cytokine levels at each time point.

Results

GFAP upregulation in the $PPT1^{-/-}$ mouse

GFAP upregulation, which precedes neuronal loss (Kielar et al., 2007; Macaulay et al., 2009), is one of the first histological changes seen in the $PPT1^{-/-}$ brain (Fig. 1*a*). Focal areas of GFAP upregulation occur in the $PPT1^{-/-}$ astrocytes beginning at 3 months of age (Fig. 1*a*, black arrows). Specifically, there is a notable increase in GFAP immunostaining throughout multiple cortical, thalamic, and cerebellar regions in $PPT1^{-/-}$ mice. As the mice age, there is a change in the intensity and distribution of GFAP immunostaining throughout these regions as well as other areas in the brain (blue arrows), including the hippocampus, striatum, and brainstem.

At higher magnification, the GFAP-positive processes of immunostained astrocytes at 3 month of age appeared to surround blood vessels (Fig. 1*a*, black arrows). However, as the mice age, there appeared to be changes in GFAP immunoreactivity within reactive astrocytes. By 5–7 months of age, the distribution of GFAP immunostaining in individual cells appeared more intense and revealed more “star-shaped” protoplasmic astrocytes with hypertrophied processes.

Another molecule often altered in reactive astrocytes concurrent with GFAP upregulation is AQP4, a prominent water channel localized to astrocytic endfeet. We performed double-labeling experiments for AQP4 and the endothelial marker PECAM (CD31), in the $PPT1^{-/-}$ and WT brains at 7 months of age (Fig. 1*b*). In the WT brains, PECAM (CD31) immunostaining demarcated the vascular bed. AQP4 immunostaining in WT brains followed the outline of the vasculature, consistent with localization to the astrocytic endfeet. This pattern of staining was disrupted in the $PPT1^{-/-}$ brains. Moreover, immunostaining for AQP4 resulted in a more diffuse pattern of staining where the localization to astrocytic endfeet appeared to be less discrete.

Accelerated INCL phenotype in $GFAP^{-/-}Vim^{-/-}PPT1^{-/-}$ mice

Both the $GFAP^{-/-}Vim^{-/-}PPT1^{-/-}$ and $PPT1^{-/-}$ mice experienced premature death mimicking a clinical feature of INCL (Fig. 2). All $GFAP^{-/-}Vim^{-/-}PPT1^{-/-}$ and $PPT1^{-/-}$ mice died by 27 weeks and 35 weeks, respectively. Furthermore, the median survival for the $GFAP^{-/-}Vim^{-/-}PPT1^{-/-}$ mice was 23 weeks of age compared with 33 weeks for the $PPT1^{-/-}$ mice. Thus, the $GFAP^{-/-}Vim^{-/-}PPT1^{-/-}$ mice died earlier than the $PPT1^{-/-}$ mice ($p < 0.001$). No WT mice and only a single $GFAP^{-/-}Vim^{-/-}$ mouse (22 weeks) died prematurely in this study.

Brain weights were used as a measure of overall brain atrophy. The brains of both the $GFAP^{-/-}Vim^{-/-}PPT1^{-/-}$ and $PPT1^{-/-}$ mice developed normally with no difference in brain weights observed at 3 months of age (Fig. 3*a*). However, by 5 months, brain atrophy was apparent in both the $GFAP^{-/-}Vim^{-/-}PPT1^{-/-}$ and $PPT1^{-/-}$ mice (Fig. 3*b*). At 6 months, there was a decrease in the brain weights of the $GFAP^{-/-}Vim^{-/-}PPT1^{-/-}$ ($p < 0.001$), $GFAP^{-/-}Vim^{-/-}$ ($p < 0.01$), and $PPT1^{-/-}$ mice ($p < 0.001$) compared with WT mice (Fig. 3*c*). The $GFAP^{-/-}Vim^{-/-}$

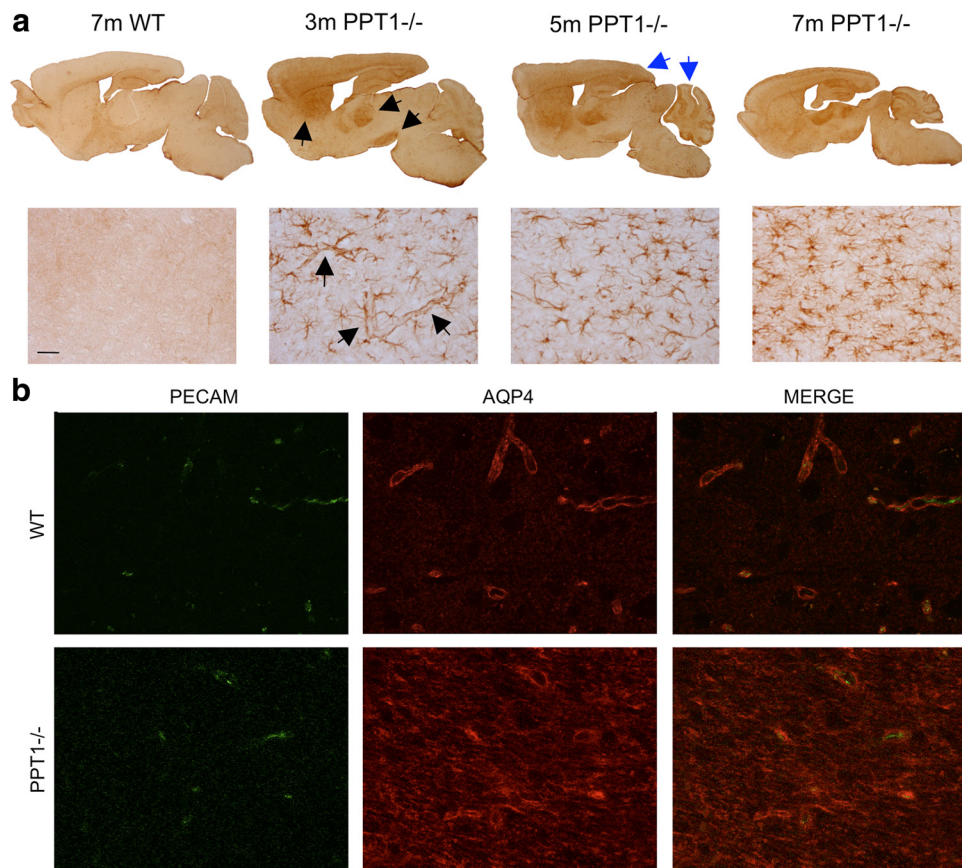


Figure 1. Reactive astrocytes in the *PPT1*^{-/-} brains. **a**, Focal regions of GFAP upregulation occur in the *PPT1*^{-/-} brain. GFAP upregulation is present in the thalamus, cortex, and cerebellum beginning at 3 months (black arrows). By 5–7 months, the intensity and distribution of GFAP immunostaining increases (blue arrows). At high magnification in the V1, the first GFAP-positive astrocytes observed at 3 months are associated with the vasculature (black arrows). As the *PPT1*^{-/-} mice age, more star-shaped protoplasmic astrocytes demonstrate GFAP immunoreactivity. Staining was absent in the 7-month-old WT brains. **b**, Immunostaining for PECAM and AQP4 in WT and *PPT1*^{-/-} brains. PECAM immunostaining outlines the blood vessels in the WT V1, which is closely associated with the AQP4 labeling of astrocytic endfeet. The pattern of AQP4 staining was disrupted in the *PPT1*^{-/-} mice. The AQP4 staining was not limited to PECAM-positive vasculature in the *PPT1*^{-/-} mice.

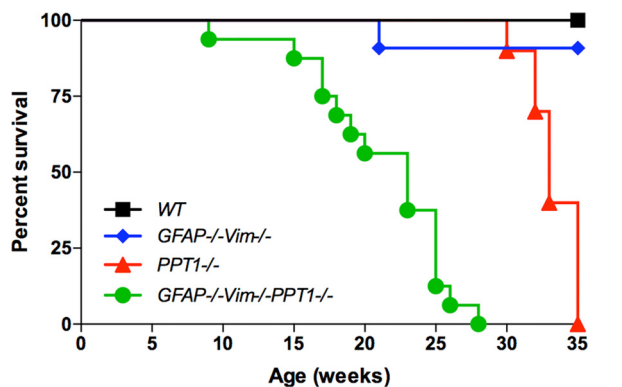


Figure 2. Lifespan of the *GFAP*^{-/-}*-Vim*^{-/-}*-PPT1*^{-/-} mice. The *GFAP*^{-/-}*-Vim*^{-/-}*-PPT1*^{-/-} mice died earlier than the *GFAP*^{-/-}*-Vim*^{-/-}, *PPT1*^{-/-}, or WT mice ($n = 10–18$ mice per genotype). The median lifespan for *GFAP*^{-/-}*-Vim*^{-/-}*-PPT1*^{-/-} mice was 23 weeks, while that for the *PPT1*^{-/-} mice was 33 weeks. Kaplan–Meier statistical analysis was used to determine differences in lifespan at the $p < 0.05$ level.

PPT1^{-/-} and *PPT1*^{-/-} brains at 6 months decreased in weight by 26.2 and 13.4%, respectively, when compared with WT brains ($p < 0.01$). The *GFAP*^{-/-}*-Vim*^{-/-}*-PPT1*^{-/-} brains weighed less than the *PPT1*^{-/-} brains (14.8% decrease; $p < 0.01$) at 6 months.

Upon gross examination, V1 of *GFAP*^{-/-}*-Vim*^{-/-}*-PPT1*^{-/-} and *PPT1*^{-/-} mice appeared atrophied compared with WT

brains (Fig. 3*d*). Therefore, we measured cortical thickness in V1 at 6 months of age in the *GFAP*^{-/-}*-Vim*^{-/-}*-PPT1*^{-/-}, *GFAP*^{-/-}*-Vim*^{-/-}, *PPT1*^{-/-}, and WT mice (Fig. 3*e*). At 6 months of age, there was a 28.9% decrease in cortical thickness of *GFAP*^{-/-}*-Vim*^{-/-}*-PPT1*^{-/-} brains compared with WT, while the *PPT1*^{-/-} brains only suffered a 21.6% loss. Therefore, cortical thinning in the *GFAP*^{-/-}*-Vim*^{-/-}*-PPT1*^{-/-} brains was more severe than in the *PPT1*^{-/-} or *GFAP*^{-/-}*-Vim*^{-/-} brains.

Accumulation of autofluorescent material throughout the neuraxis is a hallmark of INCL. To determine the level of storage material in the CNS, we quantified autofluorescence in the S1BF cortex of *GFAP*^{-/-}*-Vim*^{-/-}*-PPT1*^{-/-}, *GFAP*^{-/-}*-Vim*^{-/-}, *PPT1*^{-/-}, and WT brains (Fig. 3*f*). There was an increase ($p < 0.001$) in autofluorescent accumulation in both the *GFAP*^{-/-}*-Vim*^{-/-}*-PPT1*^{-/-} and *PPT1*^{-/-} brains (3.3- and 2.6-fold increase, respectively) when compared with WT or *GFAP*^{-/-}*-Vim*^{-/-} brains. Furthermore, there was a 1.3-fold increase in the levels of autofluorescent substrate in the *GFAP*^{-/-}*-Vim*^{-/-}*-PPT1*^{-/-} mice compared with the *PPT1*^{-/-} mice ($p < 0.001$).

Increased neurodegeneration in the *GFAP*^{-/-}*-Vim*^{-/-}*-PPT1*^{-/-} mice

Since neuronal loss is a hallmark of INCL, de Olmos cupric-silver staining was performed to assess the extent of neurodegeneration present in the *GFAP*^{-/-}*-Vim*^{-/-}*-PPT1*^{-/-} brains (Fig. 4). We compared the severity of pathology in the *GFAP*^{-/-}*-Vim*^{-/-}

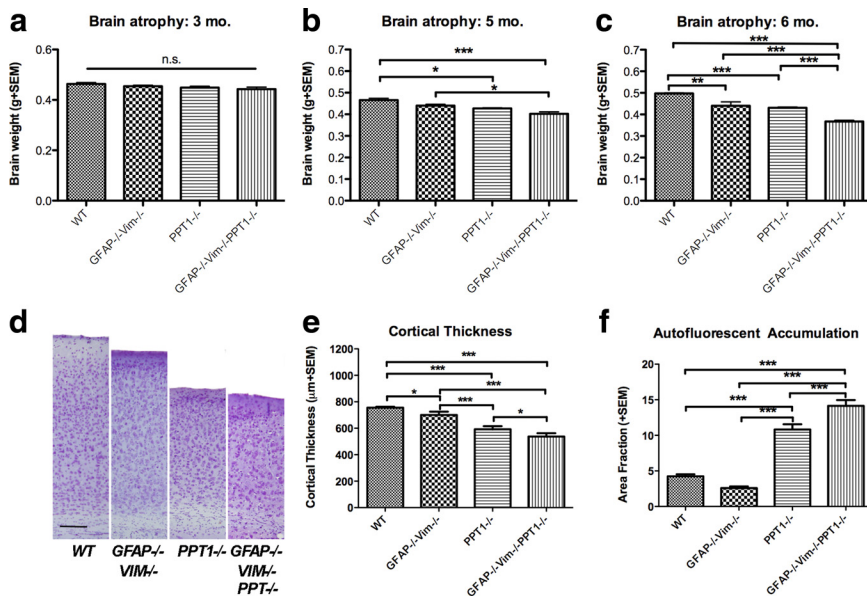


Figure 3. Accelerated disease progression in the *GFAP*^{-/-}*Vim*^{-/-}*PPT1*^{-/-} mice compared with *PPT1*^{-/-} mice. **a**, Brain weights at 3 months of age. There is no significant difference in brain weights among the *GFAP*^{-/-}*Vim*^{-/-}*PPT1*^{-/-}, *GFAP*^{-/-}*Vim*^{-/-}, *PPT1*^{-/-}, and WT mice, suggesting that brain atrophy is an age-related loss and not a developmental defect (*n* = 5–6). **b**, Brain atrophy begins at 5 months in the *GFAP*^{-/-}*Vim*^{-/-}*PPT1*^{-/-} and *PPT1*^{-/-} mice. There is a significant decrease in brain weights in the *GFAP*^{-/-}*Vim*^{-/-}*PPT1*^{-/-} and *PPT1*^{-/-} mice when compared with WT mice. No change is observed in the *GFAP*^{-/-}*Vim*^{-/-} brains compared with WT brains (*n* = 5–6 per group). **c**, Brain atrophy in the *GFAP*^{-/-}*Vim*^{-/-}*PPT1*^{-/-} mice at 6 months. The *GFAP*^{-/-}*Vim*^{-/-}*PPT1*^{-/-} brains weighed significantly less than *PPT1*^{-/-}, *GFAP*^{-/-}*Vim*^{-/-}, and WT mice (*n* = 5–6 per group). **d**, Cortical thinning in the *GFAP*^{-/-}*Vimentin*^{-/-}*PPT1*^{-/-} mice. Upon gross examination of Nissl-stained tissue, V1 of *GFAP*^{-/-}*Vim*^{-/-}*PPT1*^{-/-} and *PPT1*^{-/-} mice appeared atrophied compared with *GFAP*^{-/-}*Vim*^{-/-} and WT brains (*n* = 3 per group). Scale bar, 100 μm. **e**, Quantification of cortical thickness in the WT, *GFAP*^{-/-}*Vim*^{-/-}, *PPT1*^{-/-}, and *GFAP*^{-/-}*Vim*^{-/-}*PPT1*^{-/-} mice. The visual cortex of *GFAP*^{-/-}*Vim*^{-/-}*PPT1*^{-/-} mice was significantly thinner than that of *PPT1*^{-/-}, *GFAP*^{-/-}*Vim*^{-/-}, and WT mice (*n* = 3 per group). Interestingly, all groups displayed cortical thinning compared with WT brains (scale bar, 100 μm). **f**, Autofluorescent accumulation in the *GFAP*^{-/-}*Vimentin*^{-/-}*PPT1*^{-/-} and *PPT1*^{-/-} mice. There was an increase in autofluorescent material in the *GFAP*^{-/-}*Vim*^{-/-}*PPT1*^{-/-} mice compared with *PPT1*^{-/-}, *GFAP*^{-/-}*Vim*^{-/-}, and WT mice (*n* = 3 per group). Only significant differences as determined by one-way ANOVA followed by Bonferroni's *post hoc* tests were highlighted on the graph: **p* < 0.05, ***p* < 0.01, ****p* < 0.001.

PPT1^{-/-} mice to the *PPT1*^{-/-}, *GFAP*^{-/-}*Vim*^{-/-}, and WT mice at 5 months of age (Fig. 4*a,c*). Little or no silver staining was present in either the *GFAP*^{-/-}*Vim*^{-/-} or WT brains. Conversely, the *PPT1*^{-/-} brains showed blackened cellular profiles and axonal projections throughout the neuraxis, seen here in the hippocampus, thalamus, and cortex (Fig. 4*a*). The same pattern of staining was present in the *GFAP*^{-/-}*Vim*^{-/-}*PPT1*^{-/-} mice, but the staining was more intense when compared with the *PPT1*^{-/-} mice. Higher-magnification images showed degenerating neurons within the cortex, thalamus, hippocampus, and cerebellum of the *GFAP*^{-/-}*Vim*^{-/-}*PPT1*^{-/-} brains at 5 months of age (Fig. 4*b*). In addition to the regional distribution of neurodegeneration, we also investigated the temporal progression of disease in the *GFAP*^{-/-}*Vim*^{-/-}*PPT1*^{-/-} mice at 3, 5, and 6 months of age (Fig. 4*c*). As the *GFAP*^{-/-}*Vim*^{-/-}*PPT1*^{-/-} mice age, there is an increase in silver staining throughout the cortex, corpus callosum, hippocampus, and thalamus. Although silver staining is present in the cortex and thalamus at 3 months of age, the hippocampus is relatively spared. As the mice age, darkly stained profiles are apparent in the hippocampus as well as the cortex. Similarly, staining in the corpus callosum increases in intensity by 5 months of age. By 6 months, the intensity of staining is more intense than in a 7-month-old *PPT1*^{-/-} brain (Fig. 4*c*). In fact, the intensity of staining in the 7-month-old *PPT1*^{-/-} brain is comparable to a 5-month-old *GFAP*^{-/-}*Vim*^{-/-}*PPT1*^{-/-} brain.

Increased immune cell infiltration in the *GFAP*^{-/-}*Vim*^{-/-}*PPT1*^{-/-} mice

Sections of *GFAP*^{-/-}*Vim*^{-/-}*PPT1*^{-/-} brains stained with H&E displayed a small cell infiltrate not present in the *PPT1*^{-/-}, *GFAP*^{-/-}*Vim*^{-/-}, or WT brains (data not shown). Hypothesizing the small cell infiltrate was composed of blood-derived leukocytes, CD45 immunostaining, a pan-leukocyte marker, was performed in the *GFAP*^{-/-}*Vim*^{-/-}*PPT1*^{-/-}, *GFAP*^{-/-}*Vim*^{-/-}, *PPT1*^{-/-}, and WT brains (Fig. 5*a*). At 5 months of age, the *GFAP*^{-/-}*Vim*^{-/-}*PPT1*^{-/-} mice appeared to have more CD45-positive cells throughout the brains compared with *PPT1*^{-/-} and controls (Fig. 5*a*). No increase in CD45-positive staining was seen in the *GFAP*^{-/-}*Vim*^{-/-} mice compared with WT animals (data not shown).

At higher magnification, it was clear that the CD45-positive cells within the *GFAP*^{-/-}*Vim*^{-/-}*PPT1*^{-/-} brains were morphologically diverse (Fig. 5*b–d*, arrows). To ascertain what CD45 populations were present in the brain parenchyma, lineage-specific markers were used to identify two distinct populations. First, anti-CD3 labeling identified T cells throughout the neuraxis in both the *GFAP*^{-/-}*Vim*^{-/-}*PPT1*^{-/-} and *PPT1*^{-/-} brains but not in the WT or *GFAP*^{-/-}*Vim*^{-/-} brains (Fig. 5*e*). There was an increase in the number of CD3⁺ cells in both the *GFAP*^{-/-}*Vim*^{-/-}*PPT1*^{-/-} and *PPT1*^{-/-} brains compared with *GFAP*^{-/-}*Vim*^{-/-} or WT mice (*p* < 0.01) (Fig. 5*g*). There was no difference in cells between *GFAP*^{-/-}*Vim*^{-/-}*PPT1*^{-/-} and *PPT1*^{-/-} brains. Interestingly, the greatest increase in immune cells was observed in the monocyte population in the *GFAP*^{-/-}*Vim*^{-/-}*PPT1*^{-/-} brains (Fig. 5*f,h*). Using an anti-CD68 antibody to identify microglia and macrophages, a large population of CD68-positive cells was observed in both the *PPT1*^{-/-} and *GFAP*^{-/-}*Vim*^{-/-}*PPT1*^{-/-} brains (Fig. 5*f*). There was a 24% increase in the number of CD68-positive profiles within the *GFAP*^{-/-}*Vim*^{-/-}*PPT1*^{-/-} brains compared with the *PPT1*^{-/-} (Fig. 5*h*) (*p* < 0.001). Neither the WT nor *GFAP*^{-/-}*Vim*^{-/-} brains had an appreciable monocyte population within the brain.

Blood–brain barrier integrity of the *GFAP*^{-/-}*Vim*^{-/-}*PPT1*^{-/-} mice

To detect possible perturbations in the BBB, a quantitative EB assay was used (Fig. 6). There was no significant difference (*p* < 0.1798) in EB concentration in the *GFAP*^{-/-}*Vim*^{-/-}*PPT1*^{-/-} brains compared with WT mice, suggesting no gross perturbation of the BBB in the *GFAP*^{-/-}*Vim*^{-/-}*PPT1*^{-/-} mice. There was an increase (*p* < 0.001) in EB concentration within the brains subjected to MCAO, a positive control for BBB disruption, compared with the *GFAP*^{-/-}*Vim*^{-/-}*PPT1*^{-/-} or WT brains (Belayev et al., 1996).

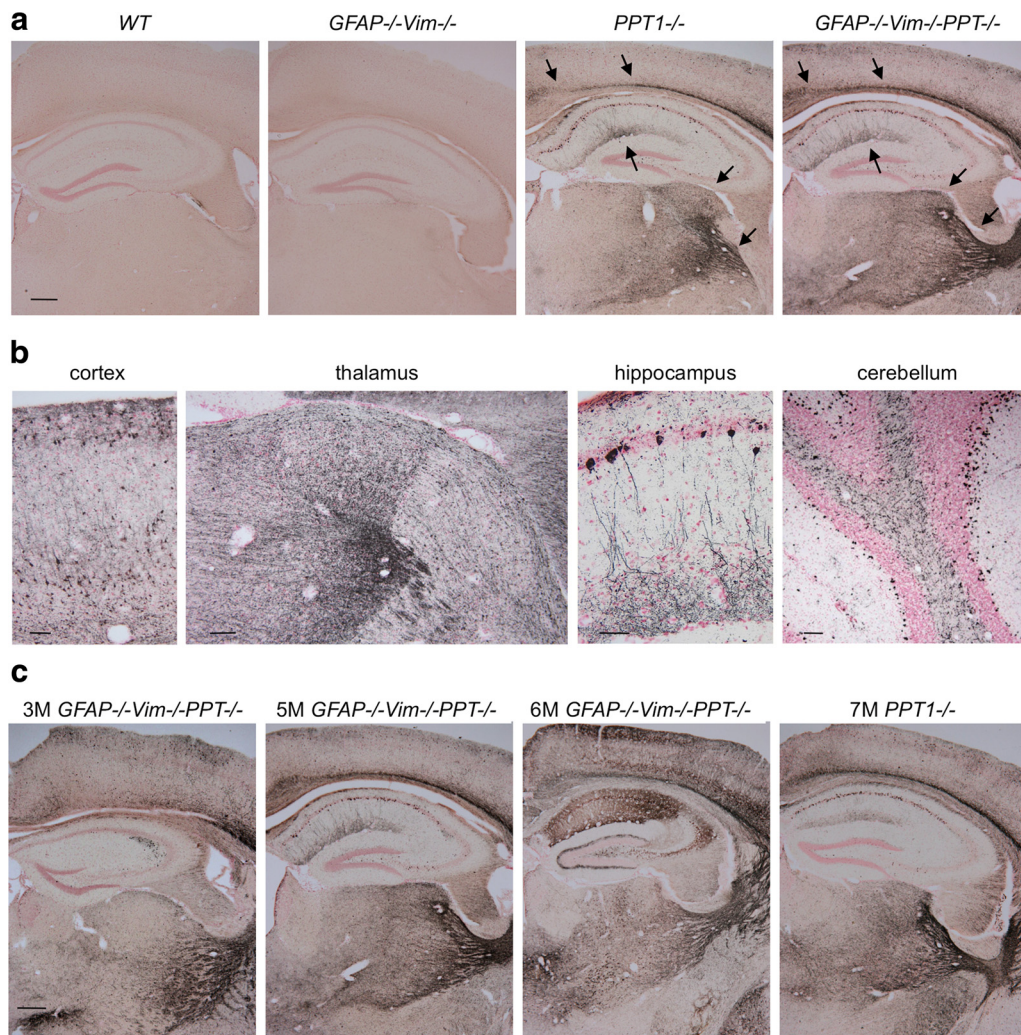


Figure 4. Neurodegeneration in the $GFAP^{-/-}$, Vimentin $^{-/-}$, and $PPT1^{-/-}$ mice. **a**, Comparison of silver staining at 5 months of age in the WT, $GFAP^{-/-}Vim^{-/-}$, $PPT1^{-/-}$, and $GFAP^{-/-}Vim^{-/-}PPT1^{-/-}$ mice. At 5 months of age, there was no staining within the WT or $GFAP^{-/-}Vim^{-/-}$ brains. Neurodegeneration in the $PPT1^{-/-}$ brain ($n = 2$) was localized to the corpus callosum, hippocampus, and thalamus (arrows). In the $GFAP^{-/-}Vim^{-/-}PPT1^{-/-}$ brain ($n = 2$), staining in these regions appeared more intense, suggesting an accelerated disease course ($n = 2$ per group). Scale bar, 300 μm . **b**, Representative images from the cortex, thalamus, hippocampus, and cerebellum of 5-month-old $GFAP^{-/-}Vim^{-/-}PPT1^{-/-}$ mice. Darkly stained cell bodies were present in the cortex (scale bar, 50 μm) and CA1 field of the hippocampus (scale bar, 50 μm), while degenerating axons are present in the thalamus (scale bar, 100 μm) and cerebellar white matter tracts (scale bar, 50 μm). **c**, Time course of silver degeneration staining in the $GFAP^{-/-}Vim^{-/-}PPT1^{-/-}$ mice. As the $GFAP^{-/-}Vim^{-/-}PPT1^{-/-}$ mice age, there is an increase in silver staining throughout the cortex, corpus callosum, hippocampus, and thalamus. Interestingly, the level of staining in a 7-month-old $PPT1^{-/-}$ brain is comparable to that observed in a 5-month-old $GFAP^{-/-}Vim^{-/-}PPT1^{-/-}$ brain and is far less than that of a 6-month-old $GFAP^{-/-}Vim^{-/-}PPT1^{-/-}$ brain. Scale bar, 300 μm .

Elevated cytokine levels in the $GFAP^{-/-}Vim^{-/-}PPT1^{-/-}$ mice

A panel of 14 chemokines/cytokines was simultaneously evaluated in 1-, 3-, and 6-month-old $GFAP^{-/-}Vim^{-/-}PPT1^{-/-}$, $PPT1^{-/-}$, $GFAP^{-/-}Vim^{-/-}$, and WT brains. The cytokines can grossly be divided into the following three groups based on function: (1) generalized proinflammatory molecules (Fig. 7*a,d,g*); (2) lymphocyte and/or monocyte activators (Fig. 7*b,e,h*); or (3) monocyte activators (Fig. 7*c,f,i*). At 1 month, there were increased concentrations of two cytokines known to act on lymphocytes and/or monocytes, RANTES and oncostatin-M, in the $GFAP^{-/-}Vim^{-/-}PPT1^{-/-}$ brains, but no changes were observed in either the $GFAP^{-/-}Vim^{-/-}$ or $PPT1^{-/-}$ brains compared with WT (Fig. 7*a–c*). By 3 months of age, 12 analytes displayed increased expression in either the $GFAP^{-/-}Vim^{-/-}PPT1^{-/-}$ or $PPT1^{-/-}$ mice compared with WT (Fig. 7*d–f*). Elevated levels of cytokine and chemokines (i.e., IFN- γ , TNF- α , oncostatin-M, lymphotactin, GM-CSF, RANTES, IP-10, MIP-1 β , MIP-2, MCP-1, MCP-3, and MCP-5) were found in the $GFAP^{-/-}Vim^{-/-}PPT1^{-/-}$ mice compared with $GFAP^{-/-}Vim^{-/-}$ or WT

mice ($p < 0.001$). Fewer cytokines and chemokines (i.e., IP-10, MCP-1, MCP-3, and MCP-5) were elevated in the $PPT1^{-/-}$ mice at the same age compared with controls ($p < 0.001$). Of the monocyte activators MIP-2, MCP-1, MCP-3, and MCP-5, there was no significant difference in cytokine levels between the $GFAP^{-/-}Vim^{-/-}PPT1^{-/-}$ and $PPT1^{-/-}$ mice. By 6 months of age, the $PPT1^{-/-}$ brains had similar levels of nearly all the cytokines listed above compared with $GFAP^{-/-}Vim^{-/-}PPT1^{-/-}$ brains (Fig. 7*g–i*). Interestingly, the concentrations of several cytokines in the $PPT1^{-/-}$ brain known to activate and recruit monocytes (Fig. 7*i*), including IP-10, MCP-1, MCP-3, and MCP-5, were higher than that of aged matched $GFAP^{-/-}Vim^{-/-}PPT1^{-/-}$ mice.

Discussion

The first histopathological change observed in the $PPT1^{-/-}$ mouse is the upregulation of the intermediate filament protein, GFAP, in reactive astrocytes. GFAP upregulation was present as early as 3 months of age in the thalamus, cortex, and cerebellum

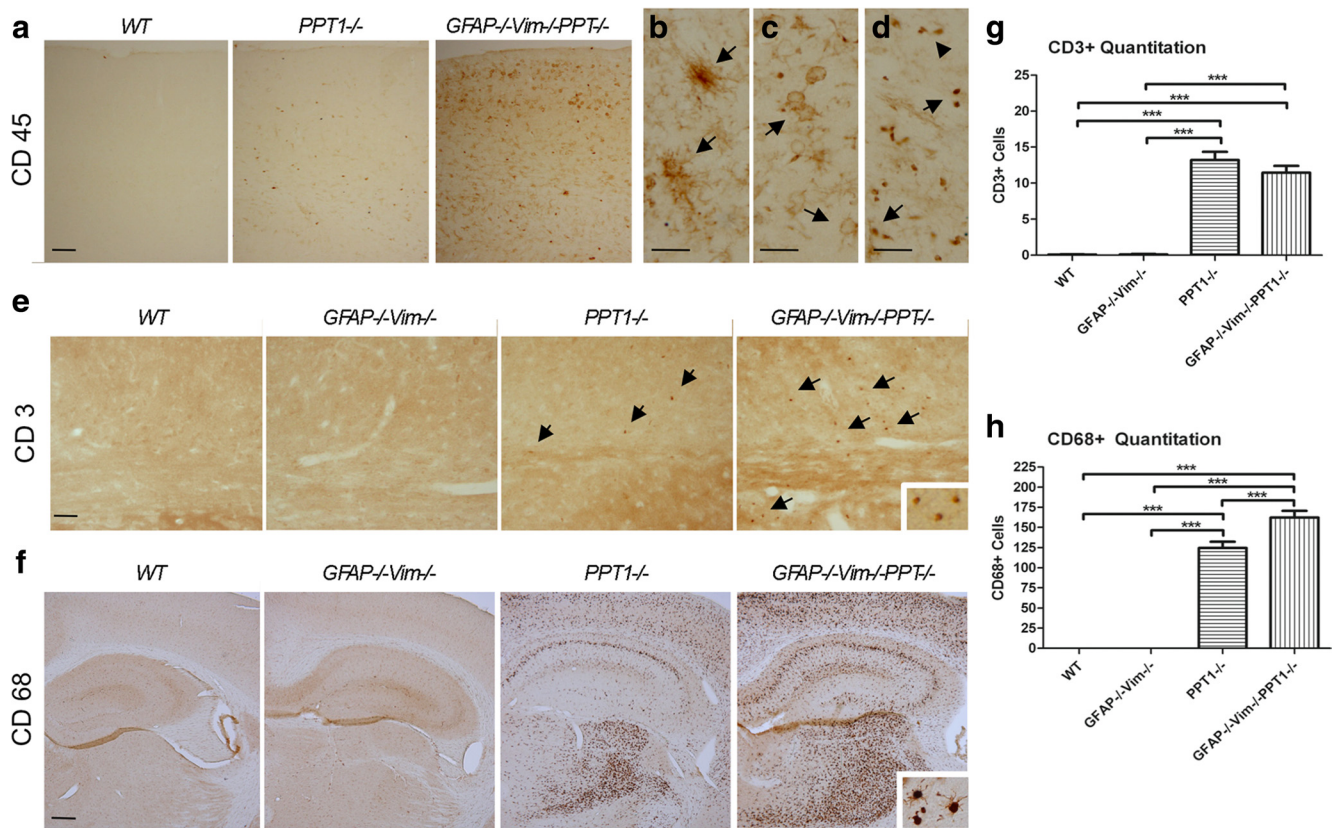


Figure 5. Immune cell infiltration into the *GFAP*^{-/-}*Vim*^{-/-}*PPT1*^{-/-} CNS. **a**, CD45, a pan-leukocyte marker, staining in the WT, *PPT1*^{-/-}, and *GFAP*^{-/-}*Vim*^{-/-}*PPT1*^{-/-} cortex. Large numbers of CD45⁺ cells were observed within the *GFAP*^{-/-}*Vim*^{-/-}*PPT1*^{-/-} cortex (*n* = 3 per group) compared with either the *PPT1*^{-/-} or WT brains. **b–d**, At higher magnification, the CD45⁺ cells appeared to be morphologically similar to microglia (**b**), granulocytes or macrophages (**c**), and lymphocytes (**d**). *GFAP*^{-/-}*Vim*^{-/-} staining was indistinguishable from that of WT. Scale bar, 30 μm. **e**, CD3⁺ immunostaining in the WT, *GFAP*^{-/-}*Vim*^{-/-}, *PPT1*^{-/-}, and *GFAP*^{-/-}*Vim*^{-/-}*PPT1*^{-/-} mice. CD3⁺ cells were found in both the *PPT1*^{-/-} and *GFAP*^{-/-}*Vim*^{-/-}*PPT1*^{-/-} mice. **f**, CD68⁺ immunostaining in the WT, *GFAP*^{-/-}*Vim*^{-/-}, *PPT1*^{-/-}, and *GFAP*^{-/-}*Vim*^{-/-}*PPT1*^{-/-} brains. Immunostaining with a CD68 antibody demonstrated a large monocyte (i.e., microglia and macrophages) population within the *PPT1*^{-/-} and *GFAP*^{-/-}*Vim*^{-/-}*PPT1*^{-/-} brains, seen here in the cortex, hippocampus, and thalamus (*n* = 3 per group). The CD68⁺ cells were composed of large macrophages and/or activated microglia (inset). **g**, Quantitation of CD3⁺ immunoreactivity in the WT, *GFAP*^{-/-}*Vim*^{-/-}, *PPT1*^{-/-}, and *GFAP*^{-/-}*Vim*^{-/-}*PPT1*^{-/-} brains. There is a significant increase in the number of CD3⁺ cells within the *GFAP*^{-/-}*Vim*^{-/-}*PPT1*^{-/-} and *PPT1*^{-/-} brains when compared with controls (*n* = 3 per group). **h**, Quantitation of CD68⁺ cells in the WT, *GFAP*^{-/-}*Vim*^{-/-}, *PPT1*^{-/-}, and *GFAP*^{-/-}*Vim*^{-/-}*PPT1*^{-/-} brains. There is a significant increase in the number of positive cells within the *GFAP*^{-/-}*Vim*^{-/-}*PPT1*^{-/-} brains when compared with *PPT1*^{-/-} mice or controls (*n* = 3 per group). One-way ANOVAs followed by Tukey's *post hoc* tests were used to determine statistical significance (***)*p* < 0.001. Scale bars: **a**, 100 μm; **b–d, f**, 300 μm.

of *PPT1*^{-/-} mice. Subsequent to this marker of early-stage astrocyte activation, there was significant neuronal loss in the same regions (Kielar et al., 2007; Macauley et al., 2009). Therefore, we hypothesized that astrocyte activation plays a role in the pathogenesis of INCL. If so, are reactive astrocytes beneficial or detrimental to the INCL brain?

In the absence of the intermediate filament proteins, GFAP and vimentin, the time course of disease was accelerated in the *GFAP*^{-/-}*Vim*^{-/-}*PPT1*^{-/-} mice compared with the *PPT1*^{-/-} mice. By all criteria measured, the *GFAP*^{-/-}*Vim*^{-/-}*PPT1*^{-/-} mice displayed either an earlier onset of the disease (i.e., premature death and brain atrophy) or an increased severity of disease at a particular time point (i.e., cortical thinning, autofluorescence, neurodegeneration, and immune cell infiltration). These data suggest that intermediate filament upregulation associated with reactive astrocytes, is a protective process in INCL. Although reactive astrocytes are responsible for both positive and negative outcomes in the CNS, our results are consistent with previous findings that use transgenic models to either ablate scar-forming astrocytes or knock out specific molecules associated with reactive astrocytes. Ablating scar-forming astrocytes (Bush et al., 1998, 1999) in models of experimental autoimmune encephalo-

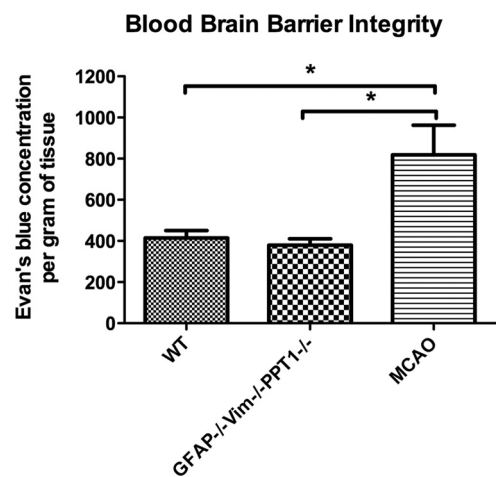
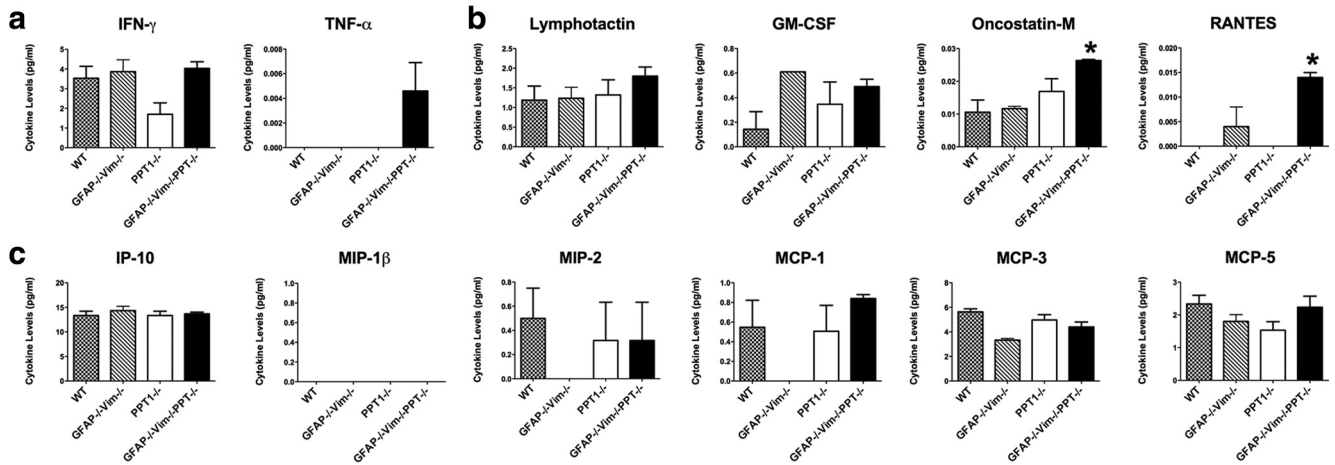
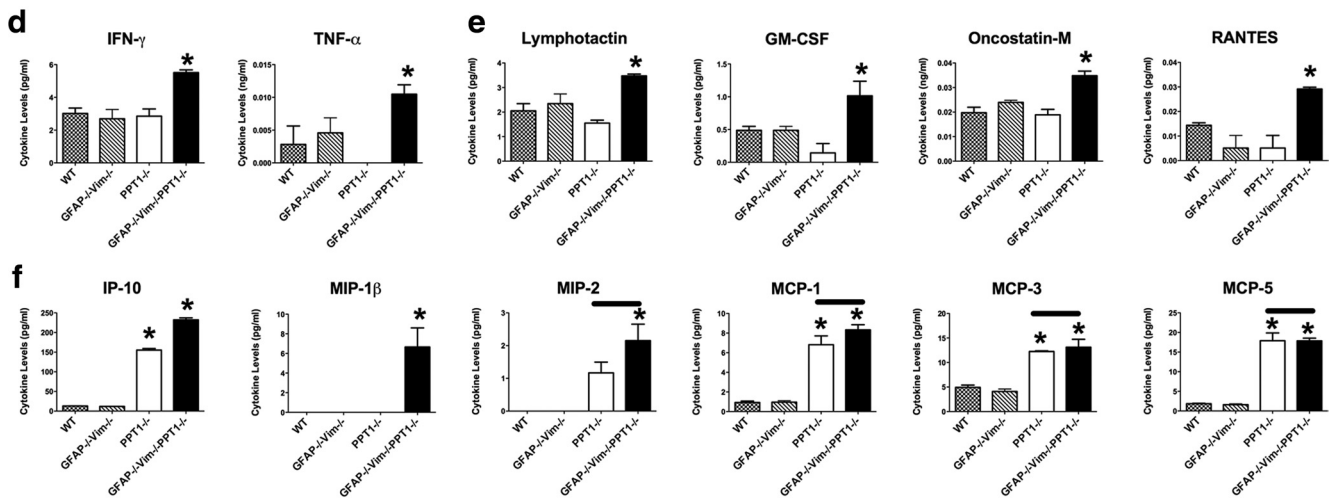


Figure 6. Blood–brain barrier integrity in the *GFAP*^{-/-}*Vim*^{-/-}*PPT1*^{-/-} mouse. An Evan's blue assay was performed to assess BBB permeability in the *GFAP*^{-/-}*Vim*^{-/-}*PPT1*^{-/-} brains compared with WT mice. There was no difference in the amount of Evan's blue/albumin complex detected in the brains of *GFAP*^{-/-}*Vim*^{-/-}*PPT1*^{-/-} compared with WT mice (*n* = 4 per group). There was an increase in Evan's blue concentration following an MCAO. Statistical differences were assessed using a one-way ANOVA followed by a Tukey's *post hoc* test (**p* < 0.05).

1 month



3 months



6 months

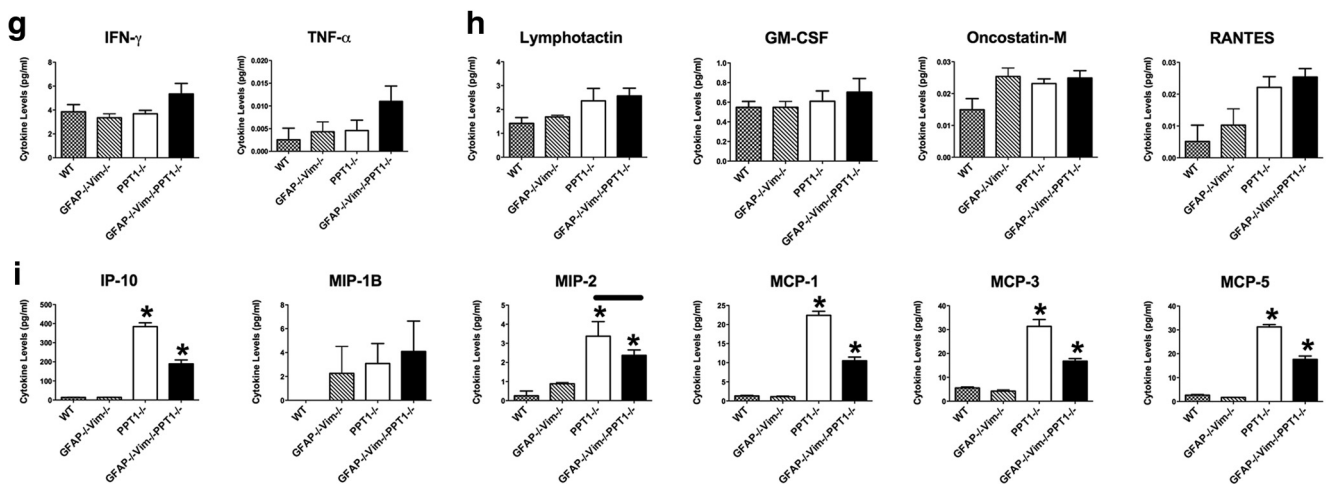


Figure 7. Elevated cytokine levels in the *GFAP*^{-/-}*Vim*^{-/-}*PPT1*^{-/-} brains at 1, 3, and 6 months of age. Of 14 cytokines assayed, the concentrations of 12 analytes were elevated at 1, 3, or 6 months of age (*n* = 3 per group). **a–i.** The cytokines can grossly be divided into three groups based on function: generalized proinflammatory molecules (**a, d, g**); lymphocyte and/or monocyte activators (**b, e, h**); or monocyte activators (**c, f, i**). **a–c.** Elevations in cytokine levels at 1 month. At 1 month, the only significant elevations in cytokine levels were observed with two lymphocyte/monocyte activators, oncostatin-M and RANTES. **d–f.** Elevations in cytokine levels at 3 months. There was an increase in all proinflammatory (**d**) and lymphocyte/monocyte (**e**) cytokines in the *GFAP*^{-/-}*Vim*^{-/-}*PPT1*^{-/-} mice at 3 months. Of the six monocyte activators (**f**) assayed, there were four molecules (i.e., IP-10, MCP-1, MCP-3, and MCP-5) increased in both the *GFAP*^{-/-}*Vim*^{-/-}*PPT1*^{-/-} and *PPT1*^{-/-} brains. MIP-1β was increased in solely the *GFAP*^{-/-}*Vim*^{-/-}*PPT1*^{-/-} brains. Although IP-10 was significantly increased *PPT1*^{-/-} brains, the levels of IP-10 were significantly higher in the *GFAP*^{-/-}*Vim*^{-/-}*PPT1*^{-/-} brains compared *PPT1*^{-/-}. **g–i.** Elevations in cytokine levels at 6 months. At 6 months, the only increase in cytokine levels observed was in analytes within the monocyte activator group. Interestingly, both the *GFAP*^{-/-}*Vim*^{-/-}*PPT1*^{-/-} and *PPT1*^{-/-} brains demonstrated (*Figure legend continues.*)

myelitis (Voskuhl et al., 2009), traumatic brain injury (Myer et al., 2006), and spinal cord injury (Faulkner et al., 2004) resulted in increased tissue damage, greater infarct size, increased neurodegeneration, increased demyelination, and exacerbated neuroinflammation. Likewise, mice lacking GFAP and vimentin that were given ischemic injury (Li et al., 2008), traumatic brain injury (Pekny et al., 1999; Wilhelmsson et al., 2004), or spinal cord lesions (Pekny et al., 1999) had increased post-traumatic recovery time, clinical outcomes, and lesion size. Although each transgenic model has a unique set of limitations for studying reactive astrocytes (i.e., neither GFAP nor vimentin is solely expressed by astrocytes), the cumulative results from these studies help further our understanding of the cellular, molecular, and functional changes associated with astrocyte activation.

In an effort to investigate the underlying mechanism causing the accelerated phenotype in *GFAP^{-/-}Vim^{-/-}PPT1^{-/-}* mice, the presence of inflammatory cells within the *GFAP^{-/-}Vim^{-/-}PPT1^{-/-}* brains was investigated. In fact, CD45⁺ leukocytes were detected in the brains of 6-month-old *GFAP^{-/-}Vim^{-/-}PPT1^{-/-}* mice, a phenomenon largely absent in the *PPT1^{-/-}* or *GFAP^{-/-}Vim^{-/-}* brains at a comparable age. Interestingly, by 7 months, CD45-positive cells were present in the brains of *PPT1^{-/-}* mice, demonstrating an aspect of neuroinflammation previously undocumented. The CD45⁺ cells within the *GFAP^{-/-}Vim^{-/-}PPT1^{-/-}* brains were morphologically diverse, containing both a large monocyte (CD68⁺) and T-cell (CD3⁺) population. We hypothesize that early activation of microglia and infiltration of both macrophages and T cells were contributing to the accelerated disease course observed in the *GFAP^{-/-}Vim^{-/-}PPT1^{-/-}* mice. Although the vimentin deficiency interferes with leukocyte and monocyte adhesion and extravasation (Nieminen et al., 2006), the addition of the *PPT1* and *GFAP* mutations appeared to counteract this effect and allow increased cell entry into the CNS.

To examine the possible mechanisms for immune cell entry into the CNS, our work focused on the blood–brain barrier. Interestingly, the astrocytes that first display an increase in GFAP immunoreactivity appear to be in intimate contact with the vasculature. Furthermore, *PPT1^{-/-}* mice appear to have aberrant PECAM and AQP4 immunostaining, suggesting alterations in the gliovascular unit. Thus, the ability of a large EB–albumin complex to enter the brain parenchyma was used to investigate BBB integrity. No gross perturbation of the BBB was appreciable in either the *GFAP^{-/-}Vim^{-/-}PPT1^{-/-}* or *PPT1^{-/-}* mice, findings similar to those previously reported in the *GFAP^{-/-}Vim^{-/-}* mice (Pekny and Wilhelmsson, 2006).

Given that the BBB is both a physical and molecular barrier, the molecular signals expressed in the CNS responsible for microglial activation and monocyte and leukocyte recruitment were investigated. At 1 month, there were elevations in two cytokines in the *GFAP^{-/-}Vim^{-/-}PPT1^{-/-}* brains compared with *GFAP^{-/-}Vim^{-/-}*, *PPT1^{-/-}*, or WT brains. Similarly, by 3 months of age, there was an increase in 12 cytokines in the *GFAP^{-/-}*

Vim^{-/-}PPT1^{-/-} brains compared with elevations in only 4 cytokines in the *PPT1^{-/-}* brains. In most cases, cytokine levels in 3-month-old *GFAP^{-/-}Vim^{-/-}PPT1^{-/-}* mice were greater than those seen in *PPT1^{-/-}* mice. Thus, this finding suggests that increased cytokine expression could not only be responsible for the influx of peripheral immune cells into the CNS, but also might provide an explanation for the accelerated neurodegeneration seen in the *GFAP^{-/-}Vim^{-/-}PPT1^{-/-}* mice. Further studies need to be performed to investigate the correlation between neuroinflammation and chronic neurodegeneration.

Cytokines with increased expression levels in the *GFAP^{-/-}Vim^{-/-}PPT1^{-/-}* brains can be clustered into three groups based on their known effects in the CNS. First, at 3 months, there were increased levels of TNF- α and IFN- γ in the *GFAP^{-/-}Vim^{-/-}PPT1^{-/-}* brains. Both of these proinflammatory molecules are often elevated in the CNS in response to acute injury or chronic disease. They are responsible for the activation and regulation of both resident (i.e., astrocytes and microglia) and infiltrating (i.e., T cells and macrophages) immune cells. IFN- γ is known to be a potent inducer of class II MHC expression in astrocytes, which is subsequently responsible for the activation of both T cells and macrophages. Furthermore, production of IFN- γ can damage the BBB due to cytotoxic effects on endothelial cells (Chavarría and Alcocer-Varela, 2004). The elevation of both TNF- α and IFN- γ in the *GFAP^{-/-}Vim^{-/-}PPT1^{-/-}* brains, but not in the *PPT1^{-/-}* brains, suggests that attenuated astrocyte activation exacerbates neuroinflammation in the CNS. Furthermore, it suggests that this is a widespread phenomenon affecting a variety of cell types in the CNS, namely astrocytes, microglia/macrophages, and infiltrating lymphocytes.

The second set of elevated cytokines in the *GFAP^{-/-}Vim^{-/-}PPT1^{-/-}* brains demonstrated the largest fold change (i.e., a 6–20-fold change). In all cases, these cytokines (i.e., IP-10, MIP1 β , MIP-2, MCP-1, MCP-3, and MCP-5) are responsible for the activation and recruitment of microglia and monocytes within the CNS. Not surprisingly, this upregulation correlated with an increase in the number of CD68-positive monocytes found within the *GFAP^{-/-}Vim^{-/-}PPT1^{-/-}* brains. These molecules are not only responsible for the recruitment and activation of monocytes, but also cause an increase in cytokine expression within these cells, propagating the neuroinflammatory process.

The final group of cytokines (i.e., oncostatin-M, lymphotactin, GM-CSF, and RANTES) is responsible for the recruitment and activation of T cells in addition to monocytes. Again, these data correlate with immunostaining of the *GFAP^{-/-}Vim^{-/-}PPT1^{-/-}* brains that demonstrate the presence of CD3-positive T cells within the CNS. One molecule, oncostatin-M, is also expressed by endothelial cells and facilitates leukocyte adhesion and rolling necessary for extravasation of cells across the blood–brain barrier. Oncostatin-M, along with RANTES, were the only two cytokines upregulated in the *GFAP^{-/-}Vim^{-/-}PPT1^{-/-}* brains at 1 month. Thus, we demonstrate molecular and cellular changes, which could increase inflammation within the CNS in the presence of attenuated astrogliosis. We believe this proinflammatory cascade is one explanation for the accelerated neurodegeneration and premature death of *GFAP^{-/-}Vim^{-/-}PPT1^{-/-}* mice.

The generation of the *GFAP^{-/-}Vim^{-/-}PPT1^{-/-}* mice helped elucidate the profound neuroinflammatory component in INCL. Although previous research described the presence of both reactive astrocytes and microglia (Bible et al., 2004; Griffey et al., 2004, 2006; Kielar et al., 2007; Macauley et al., 2009) and increased mRNA levels of a number of cytokines and chemokines

←

(Figure legend continued.) a significant increase in IP-10, MIP-2, MCP-1, MCP-3, and MCP-5. In three of the four molecules, the concentrations of cytokines were higher in the *PPT1^{-/-}* brains compared with *GFAP^{-/-}Vim^{-/-}PPT1^{-/-}* brains. Using one-way ANOVAs followed by Bonferroni's *post hoc* tests, the asterisk (*) indicates a significant increase at the $p < 0.05$ level of one group compared with all other groups, while the bar indicates no significant difference between two groups. Checked bars indicate WT, diagonal hatch marks indicate *GFAP^{-/-}Vim^{-/-}*, open bars indicate *PPT1^{-/-}*, and filled bars indicate *GFAP^{-/-}Vim^{-/-}PPT1^{-/-}* brains.

in *PPT1*^{-/-} brains (Qiao et al., 2007), the scope of neuroinflammation in INCL has largely gone underappreciated. The severity of the immune cell activation and recruitment in the *GFAP*^{-/-} *Vim*^{-/-} *PPT1*^{-/-} mice illustrates the need to further understand this pathogenic mechanism so that all aspects of CNS disease are properly targeted therapeutically in INCL.

Returning to the question, “are reactive astrocytes beneficial or deleterious in INCL?,” this study investigated the role of attenuated astrocyte activation in a mouse model of chronic neurodegeneration using the *GFAP*^{-/-} *Vim*^{-/-} mice. To date, astrocyte activation has largely been studied in models of acute trauma or injury. Findings from those studies demonstrate a complex response of both positive and negative outcomes. Our data are consistent with these previous studies in that reactive astrocytes are protective in INCL. This study is of particular interest because, in contrast to most other models used to define reactive astrocytes, INCL is one of the few models where GFAP upregulation is a widespread phenomenon, glial scarring of small lesions or infarcts is absent, CNS disease is both chronic and progressive, and the disease-causing mechanism (i.e., PPT1 deficiency) remains present for the duration of life. Given this unique set of characteristics, these data help further the understanding of reactive astrocytes in yet another example of CNS disease. This has important implications not only for our understanding and treatment of INCL, but also for our understanding of the complicated relationship between intermediate filament upregulation, reactive astrocytes, and neurodegeneration in other chronic neurodegenerative disorders, like AD, PD, or ALS.

References

- Belayev L, Busto R, Zhao W, Ginsberg MD (1996) Quantitative evaluation of blood-brain barrier permeability following middle cerebral artery occlusion in rats. *Brain Res* 739:88–96.
- Bible E, Gupta P, Hofmann SL, Cooper JD (2004) Regional and cellular neuropathology in the palmitoyl protein thioesterase-1 null mutant mouse model of infantile neuronal ceroid lipofuscinosis. *Neurobiol Dis* 16:346–359.
- Bush TG, Savidge TC, Freeman TC, Cox HJ, Campbell EA, Mucke L, Johnson MH, Sofroniew MV (1998) Fulminant jejuno-ileitis following ablation of enteric glia in adult transgenic mice. *Cell* 93:189–201.
- Bush TG, Puvanachandra N, Horner CH, Polito A, Ostendorf T, Svendsen CN, Mucke L, Johnson MH, Sofroniew MV (1999) Leukocyte infiltration, neuronal degeneration, and neurite outgrowth after ablation of scar-forming, reactive astrocytes in adult transgenic mice. *Neuron* 23:297–308.
- Chavarría A, Alcocer-Varela J (2004) Is damage in central nervous system due to inflammation? *Autoimmun Rev* 3:251–260.
- Colucci-Guyon E, Portier MM, Dunia I, Paulin D, Pournin S, Babinet C (1994) Mice lacking vimentin develop and reproduce without an obvious phenotype. *Cell* 79:679–694.
- DeOlmos JS, Ingram WR (1971) An improved cupric-silver method for impregnation of axonal and terminal degeneration. *Brain Res* 33:523–529.
- Eliasson C, Sahlgren C, Berthold CH, Stakeberg J, Celis JE, Betsholtz C, Eriksson JE, Pekny M (1999) Intermediate filament protein partnership in astrocytes. *J Biol Chem* 274:23996–24006.
- Faulkner JR, Herrmann JE, Woo MJ, Tansey KE, Doan NB, Sofroniew MV (2004) Reactive astrocytes protect tissue and preserve function after spinal cord injury. *J Neurosci* 24:2143–2155.
- Gidday JM, Gasche YG, Copin JC, Shah AR, Perez RS, Shapiro SD, Chan PH, Park TS (2005) Leukocyte-derived matrix metalloproteinase-9 mediates blood-brain barrier breakdown and is proinflammatory after transient focal cerebral ischemia. *Am J Physiol Heart Circ Physiol* 289:H558–H568.
- Griffey MA, Wozniak D, Wong M, Bible E, Johnson K, Rothman SM, Wentz AE, Cooper JD, Sands MS (2006) CNS-directed AAV2-mediated gene therapy ameliorates functional deficits in a murine model of infantile neuronal ceroid lipofuscinosis. *Mol Ther* 13:538–547.
- Griffey M, Bible E, Vogler C, Levy B, Gupta P, Cooper J, Sands MS (2004) Adeno-associated virus 2-mediated gene therapy decreases autofluorescent storage material and increases brain mass in a murine model of infantile neuronal ceroid lipofuscinosis. *Neurobiol Dis* 16:360–369.
- Griffey M, Macauley SL, Ogilvie JM, Sands MS (2005) AAV2-mediated ocular gene therapy for infantile neuronal ceroid lipofuscinosis. *Mol Ther* 12:413–421.
- Gupta P, Soyombo AA, Atashband A, Wisniewski KE, Shelton JM, Richardson JA, Hammer RE, Hofmann SL (2001) Disruption of PPT1 or PPT2 causes neuronal ceroid lipofuscinosis in knockout mice. *Proc Natl Acad Sci U S A* 98:13566–13571.
- Haltia M, Rapola J, Santavuori P, Keränen A (1973a) Infantile type of so-called neuronal ceroid-lipofuscinosis: 2. Morphological and biochemical studies. *J Neurol Sci* 18:269–285.
- Haltia M, Rapola J, Santavuori P (1973b) Infantile type of so-called neuronal ceroid-lipofuscinosis. Histological and electron microscopic studies. *Acta Neuropathol* 26:157–170.
- Hofmann SL, Das AK, Yi W, Lu JY, Wisniewski KE (1999) Genotype-phenotype correlations in neuronal ceroid lipofuscinosis due to palmitoyl-protein thioesterase deficiency. *Mol Genet Metab* 66:234–239.
- Hofmann SL, Das AK, Lu JY, Wisniewski KE, and Gupta P (2001) Infantile neuronal ceroid lipofuscinosis: no longer just a “Finnish” disease. *Eur J Paediatr Neurol* 5 [Suppl A]:47–51.
- Kalman M (2004) Glial reaction and reactive glia, Vol 31. Amsterdam: Elsevier.
- Kielar C, Maddox L, Bible E, Pontikis CC, Macauley SL, Griffey MA, Wong M, Sands MS, Cooper JD (2007) Successive neuron loss in the thalamus and cortex in a mouse model of infantile neuronal ceroid lipofuscinosis. *Neurobiol Dis* 25:150–162.
- Kohlshütter A, Gardiner RM, Goebel HH (1993) Human forms of neuronal ceroid-lipofuscinosis (Batten disease): consensus on diagnostic criteria, Hamburg 1992. *J Inher Metab Dis* 16:241–244.
- Lane EB, Pekny M (2004) Stress models for the study of intermediate filament function. *Methods Cell Biol* 78:229–264.
- Li L, Lundkvist A, Andersson D, Wilhelmsson U, Nagai N, Pardo AC, Nodin C, Ståhlberg A, Aprico K, Larsson K, Yabe T, Moons L, Fotheringham A, Davies I, Carmeliet P, Schwartz JP, Pekna M, Kubista M, Blomstrand F, Maragakis N, et al. (2008) Protective role of reactive astrocytes in brain ischemia. *J Cereb Blood Flow Metab* 28:468–481.
- Lundkvist A, Reichenbach A, Betsholtz C, Carmeliet P, Wolburg H, Pekny M (2004) Under stress, the absence of intermediate filaments from Muller cells in the retina has structural and functional consequences. *J Cell Sci* 117:3481–3488.
- Macauley SL, Wozniak DF, Kielar C, Tan Y, Cooper JD, Sands MS (2009) Cerebellar pathology and motor deficits in the palmitoyl protein thioesterase 1-deficient mouse. *Exp Neurol* 217:124–135.
- Miller BA, Perez RS, Shah AR, Gonzales ER, Park TS, Gidday JM (2001) Cerebral protection by hypoxic preconditioning in a murine model of focal ischemia-reperfusion. *Neuroreport* 12:1663–1669.
- Myer DJ, Gurkoff GG, Lee SM, Hovda DA, Sofroniew MV (2006) Essential protective roles of reactive astrocytes in traumatic brain injury. *Brain* 129:2761–2772.
- Nakazawa T, Takeda M, Lewis GP, Cho KS, Jiao J, Wilhelmsson U, Fisher SK, Pekny M, Chen DF, Miller JW (2007) Attenuated glial reactions and photoreceptor degeneration after retinal detachment in mice deficient in glial fibrillary acidic protein and vimentin. *Invest Ophthalmol Vis Sci* 48:2760–2768.
- Nieminen M, Henttinen T, Merinen M, Marttila-Ichihara F, Eriksson JE, Jalkanen S (2006) Vimentin function in lymphocyte adhesion and transcellular migration. *Nat Cell Biol* 8:156–162.
- Paxinos G, Franklin KBJ (1997) The mouse brain in stereotaxic coordinates, 2nd edition. New York: Academic.
- Pekny M, Wilhelmsson U (2006) GFAP and astrocyte intermediate filaments. In: *Handbook of neurochemistry and molecular neurobiology: neuroactive proteins and peptides* (Lajtha A, ed), pp 289–314. Berlin: Springer Reference.
- Pekny M, Nilsson M (2005) Astrocyte activation and reactive gliosis. *Glia* 50:427–434.
- Pekny M, Pekna M (2004) Astrocyte intermediate filaments in CNS pathologies and regeneration. *J Pathol* 204:428–437.
- Pekny M, Leveen P, Pekna M, Eliasson C, Berthold CH, Westermark B, Betsholtz C (1995) Mice lacking glial fibrillary acidic protein display astrocytes devoid of intermediate filaments but develop and reproduce normally. *EMBO J* 14:1590–1598.

- Pekny M, Johansson CB, Eliasson C, Stakeberg J, Wallén A, Perlmann T, Lendahl U, Betsholtz C, Berthold CH, Frisén J (1999) Abnormal reaction to central nervous system injury in mice lacking glial fibrillary acidic protein and vimentin. *J Cell Biol* 145:503–514.
- Qiao X, Lu JY, Hofmann SL (2007) Gene expression profiling in a mouse model of infantile neuronal ceroid lipofuscinosis reveals upregulation of immediate early genes and mediators of the inflammatory response. *BMC Neurosci* 8:95.
- Santavuori P, Haltia M, Rapola J, Raitta C (1973) Infantile type of so-called neuronal ceroid-lipofuscinosis: 1. A clinical study of 15 patients. *J Neurol Sci* 18:257–267.
- Santavuori P, Haltia M, Rapola J (1974) Infantile type of so-called neuronal ceroid-lipofuscinosis. *Dev Med Child Neurol* 16:644–653.
- Sofroniew MV (2005) Reactive astrocytes in neural repair and protection. *Neuroscientist* 11:400–407.
- Sofroniew MV (2009) Molecular dissection of reactive astrogliosis and glial scar formation. *Trends Neurosci* 32:638–647.
- Sofroniew MV, Vinters HV (2010) Astrocytes: biology and pathology. *Acta Neuropathol* 119:7–35.
- Switzer RC 3rd (2000) Application of silver degeneration stains for neurotoxicity testing. *Toxicol Pathol* 28:70–83.
- Verardo MR, Lewis GP, Takeda M, Linberg KA, Byun J, Luna G, Wilhelmsson U, Pekny M, Chen DF, Fisher SK (2008) Abnormal reactivity of muller cells after retinal detachment in mice deficient in GFAP and vimentin. *Invest Ophthalmol Vis Sci* 49:3659–3665.
- Vesa J, Hellsten E, Verkruyse LA, Camp LA, Rapola J, Santavuori P, Hofmann SL, Peltonen L (1995) Mutations in the palmitoyl protein thioesterase gene causing infantile neuronal ceroid lipofuscinosis. *Nature* 376:584–587.
- Voskuhl RR, Peterson RS, Song B, Ao Y, Morales LB, Tiwari-Woodruff S, Sofroniew MV (2009) Reactive astrocytes form scar-like perivascular barriers to leukocytes during adaptive immune inflammation of the CNS. *J Neurosci* 29:11511–11522.
- Wilhelmsson U, Li L, Pekna M, Berthold CH, Blom S, Eliasson C, Renner O, Bushong E, Ellisman M, Morgan TE, Pekny M (2004) Absence of glial fibrillary acidic protein and vimentin prevents hypertrophy of astrocytic processes and improves post-traumatic regeneration. *J Neurosci* 24:5016–5021.
- Young PP, Fantz CR, Sands MS (2004) VEGF disrupts the neonatal blood-brain barrier and increases life span after non-ablative BMT in a murine model of congenital neurodegeneration caused by a lysosomal enzyme deficiency. *Exp Neurol* 188:104–114.